Digital holographic interferometry with CO_2 lasers and diffuse illumination applied to large space reflector metrology

Marc P. Georges,[1,*] Jean-François Vandenrijt,[1] Cédric Thizy,[1] Yvan Stockman,[1] Patrick Queeckers,[2] Frank Dubois,[2] and Dominic Doyle[3]

[1]Centre Spatial de Liège, Université de Liège, Avenue du Pré Aily, Angleur (Liège) B-4031, Belgium

[2]Microgravity Research Centre (MRC), Université Libre de Bruxelles, CP165/62, Avenue F.D. Roosevelt 50, Brussels B-1050, Belgium

[3]European Space Research and Technology Centre (ESTEC), European Space Agency, Keplerlaan 1, Noordwijk 2200 AG, The Netherlands

*Corresponding author: mgeorges@ulg.ac.be

Received 14 August 2012; accepted 31 August 2012;
posted 25 September 2012 (Doc. ID 174310); published 1 November 2012

Digital holographic interferometry in the long-wave infrared domain has been developed by combining a CO_2 laser and a microbolometer array. The long wavelength allows large deformation measurements, which are of interest in the case of large space reflectors undergoing thermal changes when in orbit. We review holography at such wavelengths and present some specific aspects related to this spectral range on our measurements. For the design of our digital holographic interferometer, we studied the possibility of illuminating specular objects by a reflective diffuser. We discuss the development of the interferometer and the results obtained on a representative space reflector, first in the laboratory and then during vacuum cryogenic test.

OCIS codes: 090.1995, 090.2880, 120.3940, 040.3060.

1. Introduction

Coordinate and deformation metrology of complex shape space structures and reflectors is a recurrent problem addressed by space agencies and companies worldwide. Accurate knowledge of a space structure deformation or a reflector's surface shape under realistic operational conditions is essential to accurately predict in orbit performance. Consequently, suitable measurement techniques have to be developed and validated to support relevant on-ground qualification and verification testing. The application presented in this paper is related to a continuous need for the European Space Agency (ESA) to support studies of metrology for aspheric reflectors in the infrared, far-infrared and submillimeter ranges. Interest for new methods was also shown in the case of strongly asymmetric radio-frequency reflectors that depart from a global parabolic shape through localized areas of free-form curvature and that are used for producing asymmetric spot beams for specific ground coverage telecommunications. The search for adapted metrology techniques is made more complex because the reflectors can be several meters in diameter. In particular, in the project supporting our study, deformation measurements were to be demonstrated on reflectors with typical diameter of 1 m (with possible extension of the method to 4 m), with deformations ranging from 1 to 250 μm, with the highest possible spatial resolution. For that purpose we have first analyzed the potential optical noncontact methods that were available on the market or described in literature.

1559-128X/13/01A102-15$15.00/0

In general these can be grouped into two main categories: (1) those using coherent light illumination, e.g., classical interferometry [1] and holography/speckle interferometry [2], and (2) noncoherent optical techniques based on imagery, such as photogrammetry (or its recent digital videogrammetry version) [3], stereo-correlation [3,4], and fringe projection [3,5].

The second category relies on the determination of surface coordinate points from which deformations are obtained by subtracting two measurements. In the case of videogrammetry, targets have to be attached to or projected on the surface, while in digital image correlation a random pattern (made of black dots sputtered on white paint covering the object) is necessary. In fringe projection the surface has to be scattering enough to be able to observe the projected two-dimensional line pattern, which is also the case with digital image correlation using a random projected pattern. In all cases, surfaces under test have to be specially prepared, and this is not acceptable in most space testing. Indeed the surface of flight models cannot be equipped with targets nor covered by paints because the recovery of the surface would be at too high risk for the specimen. Also vacuum thermal tests generally would provoke outgassing of any paint or retroreflector targets, which has to be avoided, so preventing contamination. Despite this, videogrammetry has proven recently that it was a choice method for testing some types of space structures, making use of projected dots [6]. However, the resolution in position of points, and thus deformation, is still too low for our purpose. Indeed the resolution and measurement ranges of these techniques are influenced by the size of object, the number of pixels of the camera, and other factors specific to the technique. For examples in the best cases we found in literature for videogrammetry, resolutions of 10 parts per million (ppm) (i.e., 10 μm on a 1 m wide object) or even 1 ppm [7,8] are achievable, but a large number of measurements and camera positions are required, preventing fast single-shot captures.

The first category of interferometry methods allows fast single-shot measurements of optical phase differences between the object surface and a reference surface (classical interferometry) or between the object and itself at different instants (holographic/speckle interferometry), the resolution being driven by the laser wavelength. In classical interferometry [1], several configurations exist but generally one considers reference waves reflected by a high wavefront quality element (plane or spherical) that interfere on an image sensor with the object wave travelling independently from the test object. For testing an aspheric mirror, one has to arrange to illuminate it through diverging or converging beams, depending on the configuration. The interference between both reference and object waves leads to a fringe pattern corresponding to the localized optical path differences, where the distance between two fringes is proportional to the wavelength. When large wavefront differences are present (which is the case with aspheres illuminated by spherical wavefront), interferometers at visible wavelengths quickly show a larger fringe density than cannot be resolved for areas with large slopes. For solving this problem, interferometers at long-wave infrared (LWIR) range (e.g., 10.6 μm with CO_2 lasers) were developed in the past under various configurations like Twyman–Green [9] or Fizeau [10].

However, in the case of deep aspheric mirrors (e.g., parabola with very low f-number) like those found in space telescopes, the slope variations can still generally be too high to allow use of simple spherical illumination lenses even in LWIR. Consequently, complex custom-built null lenses need to be used instead to match the aspheric wavefront [1]. Refractive null-lens correctors are quite usual in the visible, but development of such elements can become expensive in the LWIR with the use of zinc selenide (ZnSe) or germanium (Ge) materials. Despite this, we developed in the past a high-resolution LWIR Twyman–Green interferometer [11] specifically for testing aspheric reflectors of the submillimeter Planck telescope [12,13].

Holographic interferometry (HI) is also a viable alternative used in the thermo-optical and cryogenic performance testing of space reflectors. The advantage of HI compared to classical interferometry is that it can be applied on any kind of surface provided that the object reflects some light toward the hologram sensor. Then, instead of using an expensive null lens, a simple spherical one that collects the necessary rays is sufficient.

An important point for HI is the performance of the recording medium and its ability to be used under realistic conditions (e.g., under vacuum). For continuous monitoring of large deformations, dual wavelength techniques can be envisaged but are difficult to implement [14]. The use of photorefractive crystals as a user-friendly recording medium has been intensively investigated by Centre Spatial de Liège (CSL) group [15,16]. It was then applied for a thermal-vacuum test of large reflectors [17,18], but this technique is also very sensitive to environmental disturbances that required development of specific phase stabilization techniques that were complex to implement [19]. These previous experiments motivated the study presented in this paper. Indeed the idea came to develop an HI method in LWIR that will relax the stability constraints in the setup while providing large deformation displacements in a single-shot interferogram. Given the fact that deformations to be measured on such large reflectors are ranged between 1 and 250 μm, HI in the LWIR domain imposed itself. In particular we consider digital holography (DH), which allows instant recording and readout of holograms. Although evidence of DH can be found during the early years of holography [20], it has gained a considerable interest in the past two decades due to significant improvements of electronic imaging sensors [21,22]. The technique allows numerical reconstruction of diffracted orders (among which is the image of the object of interest) through various algorithms that have been developed by many groups

[2,23–26]. All these developments were made in visible light. Recent literature presents efforts in extending DH to other spectral ranges, from the ultraviolet [27] to LWIR [28] and terahertz [29,30].

In Section 2 of this paper, we review holography in the LWIR domain. In Section 3, we present some particular aspects related to the use of thermal LWIR radiation that is of great importance to consider and that plays no role in the visible. In Section 4, we discuss the potential setup configurations necessary to observe large specular reflectors. We see that an interesting possibility is to use diffuse illumination of the specular object prior to numerical reconstruction by DH. Since this was never shown in the past, we demonstrate this principle through a series of experiments that are presented in Section 5. In Section 6, we present the DH LWIR setup for monitoring deformation of large reflectors and the results obtained in the laboratory. Section 7 presents the implementation of the setup in the cryogenic vacuum facility at the CSL and verification of the method during thermal cycling.

2. Holography with CO_2 Lasers: A Review

A. Analog Recording of Holograms with CO_2 Lasers

Holography with CO_2 lasers is not a new subject since it was first shown in 1969 by Chivian *et al.*, who used a thermochromic material (cuprous mercuric iodide) for recording at 10.6 μm and readout in the visible with an He–Ne laser [31]. Many works followed by other groups that used a similar setup and recording medium [32] or other recording media: liquid crystals [33], wax and gelatin films [34], bismuth thin films [32,35,36], acrylic and thin films [37], wax [38,39], oil films deposited on glass plates [40], resists [41], poly (acrylic acid) films [42,43], and albumen [44]. All these materials are able to record patterns through relief variations, producing phase holograms that can be processed *in situ*. Also they show relatively good figures of merit in term of diffraction efficiency. But what seems to remain limited is the resolution of such media with a rapid drop of diffraction efficiency for line spacings larger than 10 lines per millimeter. Also, they all use visible wavelengths for readout, which does not make the application of these materials for real-time HI easy. Double-exposure holograms that are readout with visible lasers have also been tried [35,40].

B. Electronic Recording of Holograms with CO_2 Lasers

The very first evidence of LWIR holographic electronic recording was provided by Løkberg and Kwon [45], who demonstrated electronic speckle pattern interferometry (ESPI) with CO_2 lasers and pyroelectric vidicon cameras. ESPI consists in recording the interference of object wave $U_o(x,y)$ and a reference wave $U_R(x,y)$ at the level of a camera focal plane. In ESPI this interference is called a specklegram, and the optical imaging system has its aperture small enough to generate speckles in the object wavefront. Also, to obtain a specklegram that can be resolved by the array sensor, the object and reference wavefronts need to match as closely as possible to each, and in-line reference beams (RBs) are used [2]. Specklegrams recorded at different instants are subtracted from each other to obtain fringe patterns that can be related to the object deformation undergone between these instants.

Applying ESPI with pyroelectric cameras is not easy since the latter are sensitive only to changes in the radiation energy. Therefore, Løkberg and Kwon worked exclusively with vibrating objects for which the speckle pattern intensity was intrinsically varying.

The second evidence of electronic recording of holograms in the LWIR was made by an Italian group who showed for the first time to our knowledge the use of DH at 10.6 μm [28]. DH is a more modern approach of holography, which consists of recording holograms directly on an imaging array sensor. In DH the intensity pattern (hologram) $I_H(\xi,\eta)$ recorded in the plane of the array sensor (ξ,η) is used to reconstruct numerically the complex object wave field $U_o(x,y)$ located in the plane (x,y) situated at a distance d from the hologram plane/sensor. If the reference complex amplitude in the hologram plane is given by $R(\xi,\eta)$, the object field is given by the Fresnel transform [23,46]:

$$U_o(x,y) = \frac{i}{\lambda d}\exp\left(-i\frac{2\pi}{\lambda}d\right)\exp\left[-i\frac{\pi}{\lambda d}(x^2+y^2)\right] \times \int_{\infty}^{\infty}\int_{\infty}^{\infty} I_H(\xi,\eta)R(\xi,\eta)\exp\left[-i\frac{\pi}{\lambda d}(\xi^2+\eta^2)\right] \times \exp\left[i\frac{2\pi}{\lambda d}(x\xi+y\eta)\right]\mathrm{d}\xi\mathrm{d}\eta. \quad (1)$$

In practice, the hologram is sampled by the array sensor on $M\times N$ pixels, of dimensions $\Delta\xi\times\Delta\eta$. Therefore, Eq. (1) can be written in a discrete form, yielding the computation of the object on $M\times N$ points, say $U_o(m,n)$, with $m=0,1,\ldots,M-1$ and $n=0,1,\ldots,N-1$. Noting the similarities between Fourier transform (FT) and Eq. (1), the computation of this field consists in applying an inverse discrete FT to the product of the three first factors under the integral of Eq. (1), say

$$U_o(m,n) = \frac{i}{\lambda d}\exp\left(-i\frac{2\pi}{\lambda}d\right) \times \exp\left[-i\frac{\pi}{\lambda d}\left(\frac{m^2}{M^2\Delta\xi^2}+\frac{n^2}{N^2\Delta\eta^2}\right)\right] \times \sum_{k=0}^{M-1}\sum_{l=0}^{N-1} R(k,l)I_H(k,l) \times \exp\left[-i\frac{\pi}{\lambda d}(k^2\Delta\xi^2+l^2\Delta\eta^2)\right]. \quad (2)$$

The authors in [23] point out that the terms outside the sum only affect the overall phase of the

object field. In a typical HI application, where we are only interested in the object deformation, these terms remain constant, and they can be neglected in the computation.

The deformation (or displacement field) is related to the phase difference between two states of the object. The phase of the object wave in every point of the object plane is given by

$$\varphi(m,n) = \tan^{-1}\left[\frac{\mathrm{Im}(U_o(m,n))}{\mathrm{Re}(U_o(m,n))}\right]. \quad (3)$$

In digital HI (DHI), one computes the phases for two consecutive states φ_1 and φ_2 of the object and subtracts one from the other to deduce the displacement. An advantage of DH over ESPI is that it allows the phase to be retrieved from a single acquisition. Another advantage of DH is that the setup does not necessitate an imaging lens in front of the sensor (like in ESPI) because the image of the object is reconstructed numerically and correct focusing of the image is obtained by setting the distance d in Eq. (2) at the same value as the one used experimentally.

DH in the LWIR was first demonstrated by Allaria *et al.* [28]. They recorded holograms in Mach–Zehnder optical configuration with pyroelectric array sensors [47] for reconstructing transmission objects. More recently the same group showed further results in measuring the three-dimensional (3D) shape of reflective objects, again with the same Mach–Zehnder configuration [48] and pyroelectric camera.

Other LWIR array sensor technologies offer advantages over pyroelectric cameras, in particular uncooled microbolometer arrays [49]. Recently George *et al.* showed DH based on a microbolometer array [50] with an optical setup similar to that of [28] and [48]. Microbolometers are now an emerging technology with a growing market and apply to thermography in many civilian, military, and industrial sectors [47,51]. Recently manufacturers have shown megapixel formats [51], which make them really attractive for developments of DH at such wavelengths.

Microbolometer arrays with medium resolutions (320 × 240 pixels) were considered in ESPI with CO_2 lasers in our early experiments with in-plane ESPI [52] and later with out-of-plane ESPI and lensless off-axis DHI [53] with the purpose of measuring large specular objects. We recently showed nondestructive testing of larger objects with a 640 × 480 pixel microbolometer camera (Variocam hr from Jenoptik) [54,55]. With the purpose of display of increasingly larger objects, the Italian group also considered medium pyroelectric array to larger microbolometer array formats (640 × 480) under several configurations [56–58].

Both groups note the interest of using such long wavelengths in DH [53,56–58] for reconstructing large objects when compared with similar setup in the visible: the maximum admissible angle between the reference and object beams is given by

$$\theta_{\max} = 2\arcsin\left(\frac{\lambda}{4\Delta}\right), \quad (4)$$

for square pixels with dimensions $\Delta = \Delta\xi = \Delta\eta$. The angle $\theta_{\max}$ sets the observable size of the object if the $+1$ diffracted orders needs to be clearly separated from other terms. When analyzing the ratio λ/Δ for visible and CO_2 wavelengths and current sensors in both domains, one easily determines that $\theta_{\max}$ is from 5 to 10 times larger in the LWIR than in the visible.

3. Particular Aspects of LWIR for DH

A. Thermal Background

The microbolometer arrays that are used in conjunction with CO_2 lasers in our experiments have a spectral sensitivity ranging from 8 to 14 μm. As is known in fundamental physics, black bodies at a given temperature emit radiation in a certain wavelength range (Planck's law) and Wien's law states that the product of wavelength of maximum spectral radiance and the temperature is a constant equal to 2.8977×10^6 nm.K.

It can be calculated that the wavelength of CO_2 lasers corresponds to ambient temperatures around 20°C. Radiation emitted by anything in the environment of work could reach the sensor directly or by reflection on either the object itself or some parts of the setup. It is then important to understand the effect of such thermal backgrounds in DH. Let us first note that this background is incoherent. Therefore, it does not participate in the building of the hologram and then cannot be propagated by DH. Nevertheless, it will appear as an additive noise component in the intensity of hologram $I_H(\xi,\eta)$. We have analyzed what a typical contribution of thermal background could be in DH. We consider a lensless DH setup [like what will be presented in Section 5 (e.g., Fig. 6)] but without either an object in the field or a laser beam switched on. Then the camera catches some radiation from the environment of the setup, as is shown in Fig. 1(a). We call the thermal contribution $I_{\mathrm{Thermal}}(\xi,\eta)$ in the plane of the sensor. When injecting this image in Eq. (2), in place of the product $I_H(\xi,\eta)R(\xi,\eta)$, and using a typical reconstruction distance d of 1 m, we obtained a central peak shown in Fig. 1(b). The extent of this peak will strongly depend on the presence of any object acting

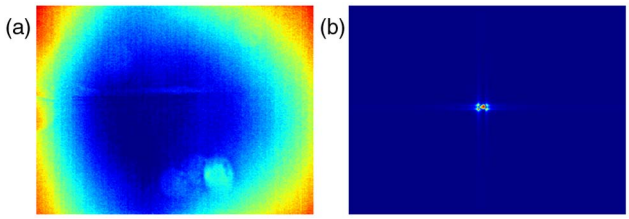

Fig. 1. (Color online) (a) Typical thermal background in an LWIR lensless DH setup and (b) contribution to the numerical reconstruction.

as heat source in the field of view, and therefore we cannot draw any generality from the example shown.

Therefore, we propose to filter this noise in the same way as other authors remove noise in DH. In all experiments presented in this paper, we apply DC-term filtering [59] as well subtraction of reference (R) and object (O) components from the hologram (H), called HRO subtraction, introduced by Skotheim for removing the halo term [60].

The HRO subtraction consists of using modified hologram intensity $I'_H(\xi,\eta)$ in place of $I_H(\xi,\eta)$ in Eq. (2) and from which images of reference and object beams, $I_R(\xi,\eta)$ and $I_O(\xi,\eta)$, respectively, are deduced. These images are captured independently by using shutters in both beams, prior to hologram capture. Here we will use the same approach but subtract also the thermal background (T) in addition to the reference and object components from the hologram H, what we will call "HROT subtraction." The intensity of the hologram to be injected in the numerical reconstruction is then given by [leaving aside the (ξ,η) dependency]

$$I'_H = I_H - I_R - I_O - I_{\text{Therm}}. \tag{5}$$

We must also take into account that the images of reference and object beams contain the same thermal background. Assuming that the latter has not changed between acquisitions, we can deduce it from the measurements of both other beams. If we add the suffix m to designate the measured images, we can write the hologram intensity to be used in the reconstruction as follows:

$$\begin{aligned} I'_H &= I_{H,m} - [I_{R,m} - I_{\text{Therm},m}] - [I_{O,m} - I_{\text{Therm},m}] - I_{\text{Therm},m} \\ &= I_{H,m} - I_{R,m} - I_{O,m} + I_{\text{Therm},m}. \end{aligned} \tag{6}$$

B. Relationship between Surface Roughness and Reflectivity

The relationship between the observed surfaces roughness and the illumination wavelength shall be considered with importance if one wishes to know with which kind of reflectivity one deals prior to developing an optical instrument. In the case of holography/speckle methods, generally having pure (diffuse) scattering reflectivity is preferred because therefore classical imaging systems can be used to focus on the object. In DH, the same is true, and a pure scattering surface will allow numerical focusing without difficulty. Working at longer wavelengths than visible will strongly impact the reflectivity type, as was already mentioned by authors working in LWIR [45]. Yamaguchi [61] has shown that, when the wavelength is close to the surface roughness or smaller, the surface becomes completely scattering and speckle appears. On the other side, specular reflection appears as soon as the wavelength is larger than the roughness and quickly dominates the speckle pattern intensity. Nevertheless, up to some extent the speckle pattern still can be observed, but its intensity is smaller than the specular peak. The total integrated scatter (TIS) represents the scattered light intensity normalized by the intensity of the reflected beam. It is proportional to the square of the ratio between the roughness and the wavelength [62]. Consequently, if the wavelength is 20 times larger, the TIS will be 400 times smaller. Thus, the speckle intensity will be 400 times smaller using a CO_2 laser than with an equivalent experiment using a visible laser. In the visible, this problem is well known, and holography/ESPI observation of surfaces having a strong specular reflection requires spraying surfaces under test with scattering powder.

We already discussed this in our earlier works [53], and for metallic surfaces with roughness in the range of a few nanometers, we dealt with this problem by spraying the surface with a white removable powder (developer for liquid dye penetrant nondestructive technique), which is largely used by holographers. In the frame of more recent works related to ESPI with CO_2 lasers for nondestructive testing on aeronautical composite structures, we measured the roughness of various materials of interest for that application and found that they were of the same order as the wavelength [63]. This allowed producing speckles in LWIR without spraying the surface, and we were able to apply DHI for successful measurement of large deformations and detection of defects in such samples [54,55].

In the intermediary cases where both specular and scattering reflectivities are observed, one has to be highly cautious to avoid specular peaks that could saturate or overload the microbolometer array, either by tilting the object (hence placing the specular peak out of the field of view of the sensor) or by spraying the surface with a diffuse scattering material [53].

4. Choice of the Most Appropriate DH Configuration

The request for our project is that the LWIR DH technique has to be adapted to aspheric reflectors, which can be either astigmatic (such as parabolas) or stigmatic (such as ellipses), with slopes that can be quite high as well as showing asymmetric slope changes (like in the case of free-form RF reflectors). Another constraint is that these reflectors can be purely specular or partially specular and scattering, as a function of their roughness and the test wavelength used. It must be noted that, most of time, these reflectors have roughness very small compared to the wavelength, yielding specular reflection.

Having this in mind, two basic cases have been distinguished in our study, which are illustrated in Fig. 2 in the case of a parabolic reflector but can be extended to other shapes. The first one considers the reflector in pure specular illumination and observation configurations [Fig. 2(a)]. The second one considers intermediary diffusers, either at the illumination stage [Fig. 2(b)] or at the observation [Fig. 2(c)]. In the figure, the illumination and observation are not coaligned, but this is for sake of simplicity.

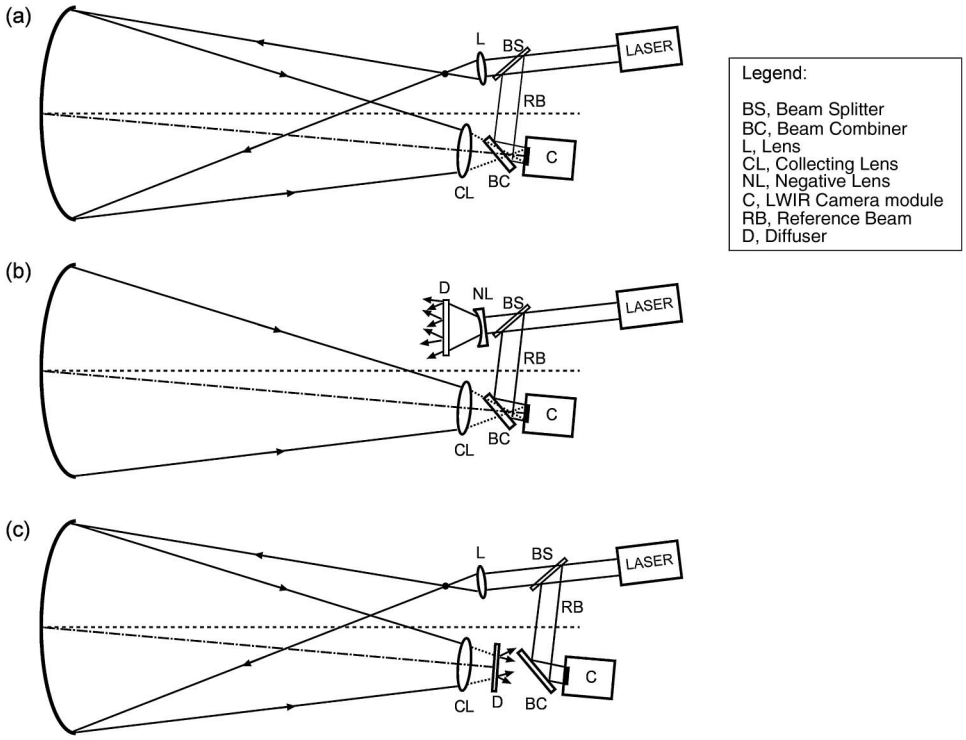

Fig. 2. Potential schemes for DH setup for large specular reflector.

The pure specular case shown in Fig. 2(a) is in fact similar to classical interferometer (of the Mach–Zehnder type) and makes use of illumination through a spherical lens with the point source at typically two times the parabola focal length. In this case rays do not converge in a single point, and a collecting lens (CL) is necessary to intercept the external rays prior to make them interfere with the RB through the beam combiner (BC). The diameter of CL has to be adapted to the optics under test without being necessarily matching perfectly the object wavefront, as would be the case with dedicated null lenses. This non-perfect-matching between the object and RB is not a problem for DH since the technique allows the reconstruction of different parts of the object by adapting the distance d in the numerical reconstruction process.

The second case, presented in Fig. 2(b), makes use of diffuse illumination produced by enlarging the object beam (here with a negative lens), which illuminates a transparent ground glass diffuser, generating a speckled wavefront, which is then reflected by the specimen. This principle has been already demonstrated in HI and ESPI for testing specular objects in visible wavelengths [64–66] and also in the case of transparent objects (for fluid convection analysis) [67]. The scattered light reaches the mirror, which reflects all rays specularly. Part of these rays reaches the camera through the imaging system. These authors note that the imaging system should be focused on the specular object to achieve maximum of contrast in the fringes [65]. Here the CL can be either an imaging lens or any lens to ease collection but not necessarily imaging the object. Alternatively, no collection lens could be used. In any case, the DH reconstruction algorithm has to be adapted to the situation.

In the third case, the illumination is similar to the pure specular case in Fig. 2(a) but the rays are directed on a diffuser which acts as an intermediary scattering object for DH. We already have used such approach with HI using photorefractive crystals [17,18] at 532 nm for measurements of smaller deformations.

We have analyzed the different scenarios and made a trade-off between the pure specular and the scattering cases. In the specular case, we computed by ray tracing the spot sizes that are obtained with typical parabolic reflectors of interest, taking into account realistic figures of slopes provided by the ESA. It appears that, apart from some examples, the spot size is often too large for the state-of-the-art detectors when no CL is used. In other cases, lenses needed to be built to either illuminate and/or collect light in the case of very large aperture (e.g., for elliptic reflectors). Despite this limitation, the specular case is expected to provide the best interference quality (like in classical interferometry) since it is not disturbed by speckle.

As mentioned above, similar setups of HI and ESPI have been demonstrated at visible wavelengths, making use of ground glass transmission diffusers. Nevertheless, transmission diffusers made of infrared transparent material (ZnSe, Ge) for working with CO_2 lasers were not found on the market and had to be custom made. Therefore, we envisaged using roughened metal plate reflecting diffusers. On that basis we kept the principle depicted in

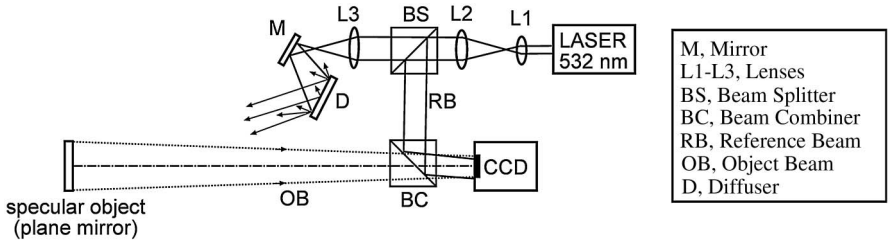

Fig. 3. Setup at 532 nm for studying DH on specular object illuminated by a reflective diffuser.

Fig. 2(b) and not Fig. 2(c). Indeed the design of the setup appeared easier with a diffuser replacing a folding mirror in the illumination arm than in the observation, specifically in view of incorporation in our vacuum facility.

Although we did not suspect any counterindication to apply such schemes to DH in LWIR, we have performed simple experiments for checking the validity of using diffuse illumination in DH, prior to full scale implementation. This is presented in detail in Section 5.

5. Diffuse Illumination in DH for Specular Objects

A simple experiment for demonstrating the possibility of using diffuse illumination with DH has first been set up in visible light as shown in Fig. 3. A diode-pumped solid-state laser at 532 nm is first expanded, and part of the collimated beam (RB) is reflected by a beam splitter (BS) and directly travels to a CCD camera after reflection by a BC. Another part of the laser beam is transmitted by BS and is further expanded and folded to reach a reflective diffuser D. The latter consists of a metallic plate roughened by sanding. Although we have not measured its roughness, we can say that it reflects partially specularly and diffusively. The setup configuration is a lensless Fresnel DH setup with off-axis RB. The size of the object has been limited, and the angle between reference and object beams has been chosen for having good separation of the different terms at the reconstruction. Fig. 4 shows the result of the numerical reconstruction [Fig. 4(a)], the masked image of the focused object selected [Fig. 4(b)], and a zoom of the speckle pattern located in the plane of the mirror object [Fig. 4(c)]. It can be seen that the average intensity of the speckle image is not homogeneous. This is because the surface of the diffuser was partially specular and a perfect Lambertian scattering profile proved difficult to obtain by means of a sanding process.

We have analyzed the behavior of the speckle pattern when the mirror object is rotated and for different distance of DH reconstruction. Fig. 5 shows the zoomed speckles in two situations. The first one [Fig. 5(a)] concerns the case of correct numerical focusing; i.e., the hologram is reconstructed with distance d equal to the true distance between the specular object and the sensor plane. The second one [Fig. 5(b)] concerns out-of-focus reconstruction. Each shows speckle grains of which positions are compared before and after rotation, left and right images, respectively. In the case of correct numerical focusing, when the mirror object is rotated out of plane, no speckle movement appears. The only variations are intensity changes of speckle grains. On the contrary, in the case of incorrect numerical focusing, speckle movement is observed during object rotation. This should cause decorrelation degrading the fringe visibility, as was observed by Hansen with HI and ESPI using an imaging lens [65,66].

On the basis of this first experiment in the visible, we settled a similar setup with a CO_2 laser and a microbolometer array camera to perform displacement field metrology on a specular surface (Fig. 6). The beam from the CO_2 laser (from the VM-TIM company, emitting 8 W at 10.6 μm) is split in two parts by a BS that reflects 90% of the beam and transmits 10% (ratio $R90/T10$). The transmitted part is the RB that is folded, expanded, collimated, and then directed onto the microbolometer camera through the BC. The latter is a Jenoptik Variocam hr camera module (640×480 pixels, pixel size $\Delta = 25$ μm) without objective lens attached. The BC is a $R50/T50$ BS. Both BS and BC are BSs made of ZnSe glass with suitable coating. The beam reflected by BS is expanded and folded to illuminate the diffuser. The latter is made

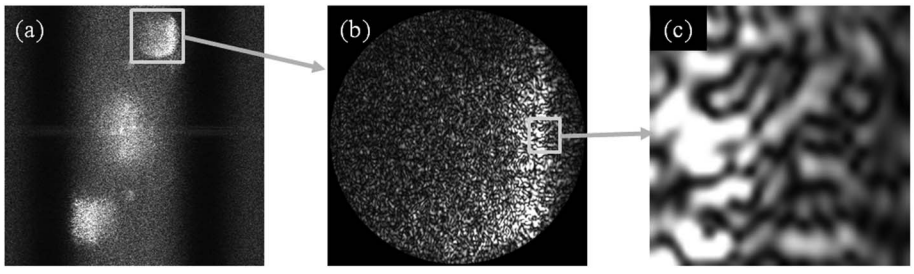

Fig. 4. (a) Numerical reconstruction of the hologram, (b) masked object at focused position, and (c) zoom of speckle located on the specular object.

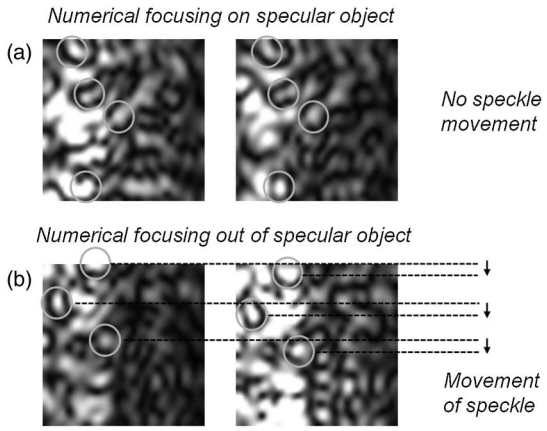

Fig. 5. Observation of speckle (zoomed image) reflected by a specular object rotated out of plane: (a) DH reconstruction correctly focused on specular object and (b) DH not correctly focused.

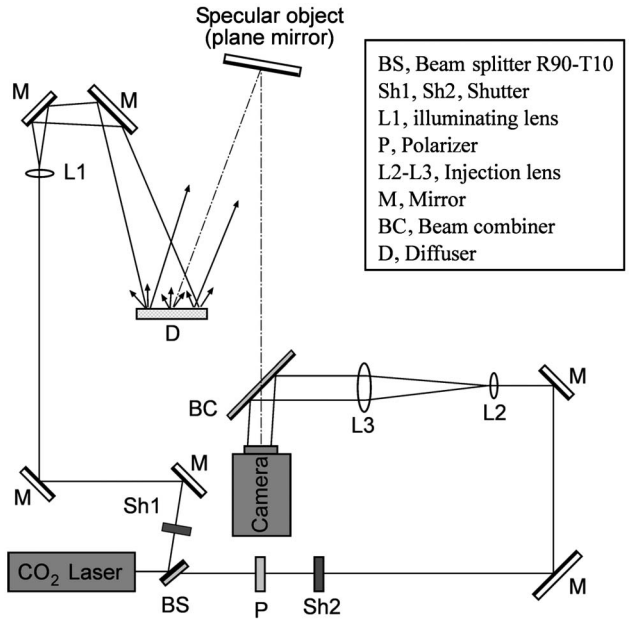

Fig. 6. Setup for studying DH in LWIR on specular object illuminated by a reflective diffuser.

of a metallic plate (Invar) that is coated by a scattering powder yielding generation of speckle that can be resolved after reflection onto the specular object. The object is a plane mirror (80 mm diameter) coated with aluminum mounted on a rotation stage for performing well-controlled out-of-plane rotation (tilt). Since the laser is polarized, the setup also includes a polarizer *P* that allows the reduction of the RB power and then equalizing reference and object beam intensities at the level of the array sensor for maximizing the hologram contrast. The angle between both beams has been arranged to allow off-axis DH and clear separation of diffracted orders.

Fig. 7(a) shows the result of DH reconstruction in amplitude, and Fig. 7(b) the same after applying filtering of DC term [59] and HROT subtraction explained in Section 3.A. To apply the HROT subtraction, one must record separately the thermal background and object and RBs independently to one another during a preliminary step, which is possible by adding shutters placed in the object and reference arms, Sh1 and Sh2 in Fig. 6, respectively. Figure 7(c) shows the difference of the reconstructed phases obtained after rotation of the mirror. Figure 7(d) shows the useful part of the mirror from which we deduced the displacement, knowing the geometry the rotation angle.

To perform analysis of the metrological performances of the technique, we have used a commercial interferometer from HP (model 5519A) for simultaneous high-accuracy measurement of the rotation angle by attaching necessary retroreflecting elements to the rotation stage of the test reflector. We varied the angle and captured the hologram and subsequently performed computation of the angle from the recovered phase differences. The angles obtained by DHI are plotted, in Fig. 8, as a function of those measured directly by the HP interferometer, as is shown. These measurements show a good agreement except for higher angles where the fringes cannot be resolved anymore. The measurement uncertainty of the commercial interferometer is 0.1 arc sec and corresponds to a displacement of 0.036 μm for the tested mirror. Therefore, one can consider that the difference between the measurement performed by the DH with diffuse illumination and the commercial interferometer corresponds to the uncertainty of the DH method. These results allowed us to determine that the uncertainty of DH is 1.5 μm as long as the number of pixels per fringes is higher than 13.

It must be noted that, if the diffuse illumination works well with small plane objects, it can become more difficult to apply with large mirrors, especially

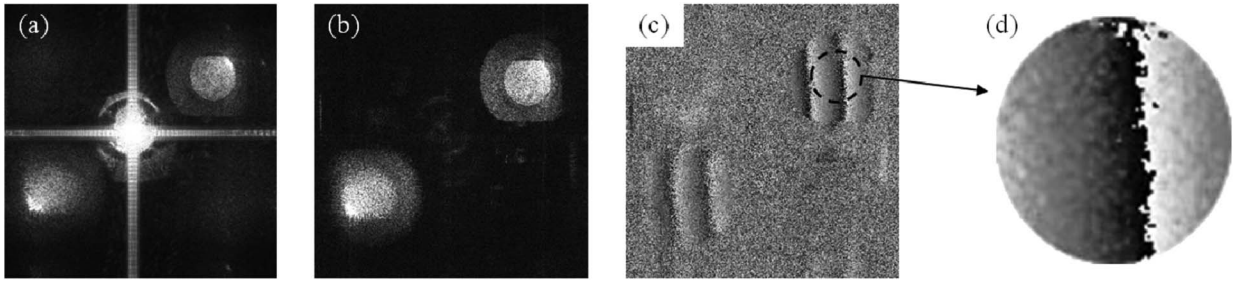

Fig. 7. Numerical reconstruction of a plane mirror by DH in the LWIR: (a) amplitude, (b) amplitude after filtering of DC term and HROT, (c) phase difference after rotation of mirror, (d) excerpt of phase difference on the mirror zone.

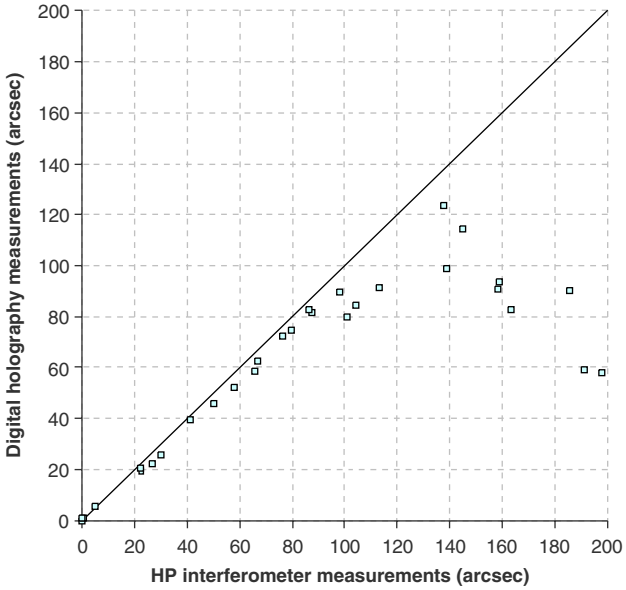

Fig. 8. (Color online) Comparison between the measurements of rotation angle from LWIR DHI of a mirror illuminated by reflective diffuser and those measured directly on the same mirror using a commercial interferometer.

Fig. 9. (Color online) FIRST demonstration reflector on its mount.

convex ones, or with specular surfaces with arbitrary shapes. In the cases of interest in our applications, we most often have to test concave mirrors, which are probably the easiest ones to deal with, even with very large reflector sizes.

6. DH Setup for Observation of Aspheric Reflectors

The test specimen that is used in the experiment is a demonstration reflector of the ESA space mission HERSCHEL [68]. Technological demonstrators of submillimeter reflectors were developed during early studies of the mission (earlier named FIRST, for Far InfraRed and Submillimetre Telescope), and one of them is considered for demonstration of our technique, as was also the case in previous developments [17,18]. The test object (Fig. 9) is a concave parabola made of a carbon fiber reinforced plastic structure with gold coating. It has a diameter of 1.1 m and focal length $f = 1.58$ m.

As already discussed, we selected a scheme corresponding to Fig. 2(b), with diffuse illumination provided by a reflective scattering plate. To limit aberrations, it is preferable to work with illumination and observation in line. Therefore, the design is based on a Mach–Zehnder configuration and is shown in Fig. 10. The elements of the drawings are at the same scale except the reflector, of which size and distance to the setup are reduced, as well as the least confusion circle (LCC), which is drawn larger that actual size. The laser beam is expanded by combination of lenses L1–L2. The beam is split in two by the beam splitter BS1 ($R1/T99$). The transmitted part is expanded by lens L3 and illuminates the reflective diffuser D. The latter is an Invar plate that is covered by white scattering powder already discussed in Section 5 and that has a roughness of typically 4 μm. This makes the diffuser partially specular and scattering. It is placed at 45° incidence, which folds the beam toward beam splitter BS2 ($R50/T50$), which in turn illuminates the reflector. The diffuser is placed at around $2f$, i.e., 3.16 m, and the parabola reflects the beam backward in the direction of BS2. The rays are focused in a blur spot (LCC). A ray tracing allowed location of the LCC near $2f$, at 3.194 m from the reflector. This spot could be located directly at the sensor S position and superposed to the RB. However, as is shown in the figure, we placed a relay system formed by combination of lenses L4 and L5. Therefore, the LCC is imaged on the array sensor of the camera. The reason for this addition is twofold. First, it allows resampling of the object image to adapt its size to the detector by adjusting the focal length ratio between L4 and L5. Second, it is related to the implementation of this setup in a vacuum chamber, which we will present in Section 7. Because both the laser and the LWIR camera are not vacuum compatible, they have to stay out of the chamber and beams have to pass through LWIR windows of which thickness must be adequate to avoid bending and failure due to the pressure difference. In function of these constraints and other ones related to the geometry of the vacuum chamber access flange, the only position for these windows is as shown by the dotted line in Fig. 10. One window will be placed in the enlarged collimated beam between L2 and BS1, and a second one between L4 and L5.

The RB is formed by the part of the beam reflected by BS1. It is first made incident to a mirror mounted on a piezo translator (MPZT), which reflects it backward through BS1 and the BC ($R50/T50$), which in turn reflects it partly onto the sensor. A lens L6 is placed in the collimated RB and forms an afocal

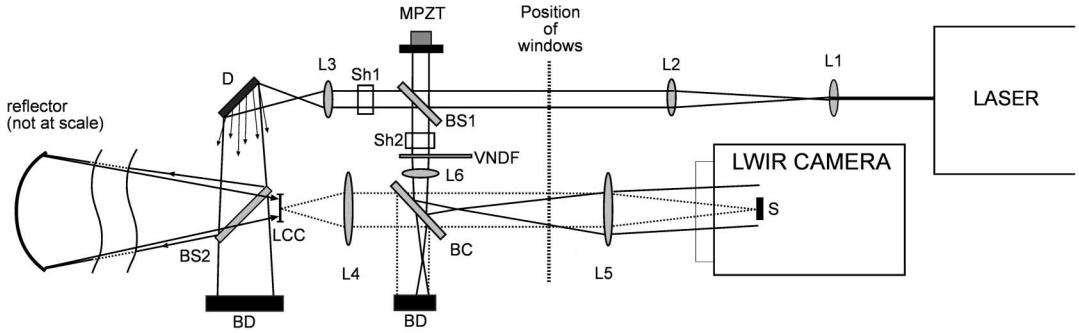

BS1-BS2, Beam splitters	L1-L6, Lenses
BC, Beam combiner	VNDF, Variable neutral density filter
D, Diffuser	MPZT, Mirror on piezo translator
Sh1, Sh2, Shutter	BD, Beam dumps
S, Array sensor	LCC, Least confusion circle

Fig. 10. Final design of the LWIR DH interferometer with diffuse illumination for large space reflector.

system with lens L5 in such a way the RB is collimated on the sensor. The RB can be made incident at an adequate angle on the sensor for applying off-axis DH. A variable neutral density filter is placed in the reference arm for equalizing the intensities of object and RBs on the sensor. Two beam dumps are placed in transmitted beams which are not used in the setup. At last two shutters (Sh1 and Sh2) are used for separate acquisition of object and reference images for filtering noise in the image, as discussed earlier in the paper.

It is possible to calculate analytically the maximum size of the object from the sampling requirements as well as the geometry of the object and RB. For that, we followed an approach similar to [69] where the authors considered the case of in-line Fresnel DH. Here we apply it to off-axis DH. First, let us consider that the sensor with pair L4–L5 in front is equivalent to a lensless system because it only acts as relay imagery from the LCC to the sensor (with possible magnification). Therefore, we have a recording situation depicted in Fig. 11 where the object is the LCC and rays from the object interact with the RB, which is collimated and is oriented to avoid overlapping of reconstructed orders. We can determine the largest angle θ between the object and RBs. As is shown in Fig. 11, this angle is formed by the ray issued from the lowest point of the LCC and reaching the highest point of the sensor S, on the one side, and the lowest ray of the RB on the other side. The maximum value of this angle $\theta_{\max}$ is deduced from the sampling theorem and given by Eq. (4), which can be simplified in the case of small angles to $\theta_{\max} = \lambda/2\Delta$. The pixel dimension of the Variocam is $\Delta = 25$ μm, which gives a maximum angle of 0.212 rad. From Fig. 11, it comes that the size of the object is related to this angle by

$$\frac{L + N\Delta}{2d} = \tan\frac{\theta}{2} \approx \frac{\theta}{2} = \frac{\lambda}{4\Delta}, \tag{7}$$

from which we find that the maximum size of the LCC is

$$L_{\max} = \frac{\lambda d - 2N\Delta^2}{2\Delta}. \tag{8}$$

Since L4 and L5 can have different focal lengths, f_4 and f_5, respectively, they can be used for optimizing the sampling of the object image to benefit as much as possible of the sensor resolution. If we define the sampling interval in the plane LCC by $\Delta' = (f_4/f_5)\,\Delta$, the size of the object $L'_{\max}$ is now given by

$$L'_{\max} = \frac{\lambda d' - 2N\left(\frac{f_4}{f_5}\Delta\right)^2}{2\left(\frac{f_4}{f_5}\Delta\right)}, \tag{9}$$

with d' the distance between LCC and the reflector of which value was found by ray tracing to be equal to 3.194 m. With equal focal lengths for L4 and L5 and considering $N = 480$, it is found that $L'_{\max} = 0.665$ m. This value is smaller than the actual size of the reflector, which is 1.1 m. Therefore, we will have an overlap of the reconstructed orders. For avoiding this, we can use different focal lengths

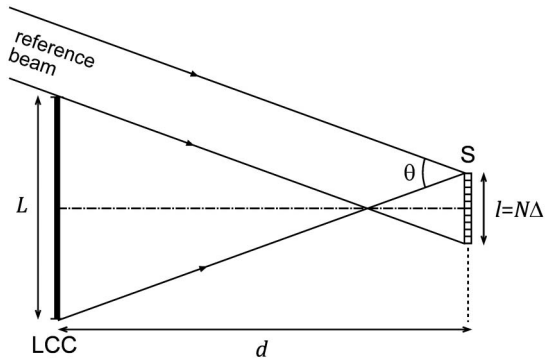

Fig. 11. Geometry of the DH recording setup.

for the pair L4–L5. We found stock ZnSe lenses with $f_4 = 75$ mm and $f_5 = 127$ mm, which gives $L'_{\max} = 1.139$ m and is compatible with the reflector.

Although the image and its conjugate are well separated under these conditions, the resolution of the useful image is not maximized because it occupies one quadrant of the detector, i.e., maximum 240×240 pixels, which is poor. To maximize the spatial resolution, we have another possibility, which is to allow overlapping orders and using the phase shifting to separate orders [70], which is typical to the in-line DH configuration. The phase-shifting technique has been implemented in the setup by means of the MPZT (in Fig. 10). Several images are recorded in sequence between which the mirror is shifted perpendicularly to the beam to create a piston effect between the images. This technique has the disadvantage that it takes a longer time for capture compared to the single-shot capability of off-axis DH. Moreover, it further imposes some stability in the setup during the acquisition sequence. Therefore, we lose the interest of off-axis DH and its possibility to access the phase of high-speed phenomena in single shot. Nevertheless, in the case of cryogenic tests, as presented in the Section 7, the temperature changes are quite slow and the acquisition times can be considered extremely small in comparison. From equations similar to Eq. (9) but dedicated to the in-line case [69], we calculate that, with $f_4 = f_5$, we obtain $L'_{\max} = 1.34$ m. Figure 12 shows the results obtained after application of this technique to reconstruct the parabolic reflector, both in modulus [Fig. 12(a)] and in phase difference [Fig. 12(b)] after an out-of-plane rotation is applied to the reflector. It must be noted that the object is not on the same optical bench than the DH setup. Despite this, we were able to capture holograms without difficulty and with perturbations in the laboratory (vibration and equipment noise, people circulating, etc.), whereas this was not possible with interferometers in the visible.

7. Application in Cryogenic Test

Following the laboratory validation, the interferometer has been implemented in the FOCAL5 vacuum chamber of the CSL [71] to measure the deformation of the reflector at cryogenic temperatures. The facilities of the CSL are all equipped with optical benches that are standing on a seismic block disconnected from the building and the vacuum chamber itself. The throughputs of the feet of the optical bench are especially designed to not allow for leakage when the vacuum is made into the chamber. Such optical benches are a prerequisite for interferometric monitoring of large specimens because they damp any vibration coming from the building or outside. The chamber has a 5 m diameter and is 10 m long. It is fully equipped with nitrogen and helium circulation circuits with regulation for reaching specific temperature sequences on specimens.

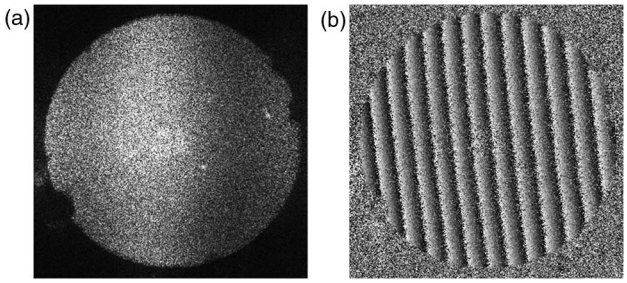

Fig. 12. Application of phase-shifting DH to the FIRST reflector with diffuse illumination. (a) Modulus and (b) phase difference after out-of-plane rotation of the reflector.

The configuration of the thermal-vacuum test uses the same optical configuration as in Fig. 10. However, the optical setup has been split in two parts, as shown in Fig. 13. The first part is outside the vacuum chamber (outer bench) and holds the vacuum-incompatible equipment (i.e., the laser and the thermographic camera). The second part (inner bench) is inside the chamber and contains the interferometer. The separation and combination of the object beam and RB is realized in the chamber to minimize the impact of differential vibration between the inner and outer bench. The dimensions of the optical setup (inner and outer benches) are exaggerated with respect to the facility and reflector dimensions. Also, the DH setup is drawn vertically, whereas it is actually horizontal. The reflector is located at the adequate distance from the interferometer and surrounded by a thermal shroud. The latter is made of copper plates painted in black on their inner part and connected to nitrogen circulation pipes. The shroud allows changing the temperature on the reflector through radiative transfer, and it is completely closed except for a small aperture for the beams to reach the reflector and be reflected backward to the DH setup.

Several thermal cycles were operated and the holograms were captured on a regular basis. Numerical reconstruction was performed, and the phase difference was computed between pairs of temperature states during the cycle.

The measurement of the displacement field for a temperature variation from 224 K (where the initial digital hologram is recorded) down to 107.5 K of the reflector is shown in Fig. 14: Fig. 14(a) is the raw phase difference, Fig. 14(b) is the masked region of interest obtained after applying a median filtering on Fig. 14(a), and Fig. 14(c) is the unwrapped phase [2] from which the displacement field can be deduced [2]. Figure 14(d) shows the total displacement field, and Fig. 14(d) (Media 1) shows the displacement evolving in function of temperature. We are interested in the deformation that is obtained by removing the rigid body motions from the total displacement field. These are tilts and defocus that were removed from the phase by Zernike analysis [1]. The remaining result is shown in Fig. 15(b).

For validating the performance of the LWIR DH interferometer, the results have been compared to measurements made on the same reflector some years before, with a high spatial resolution LWIR interferometer also developed at CSL [11] and which

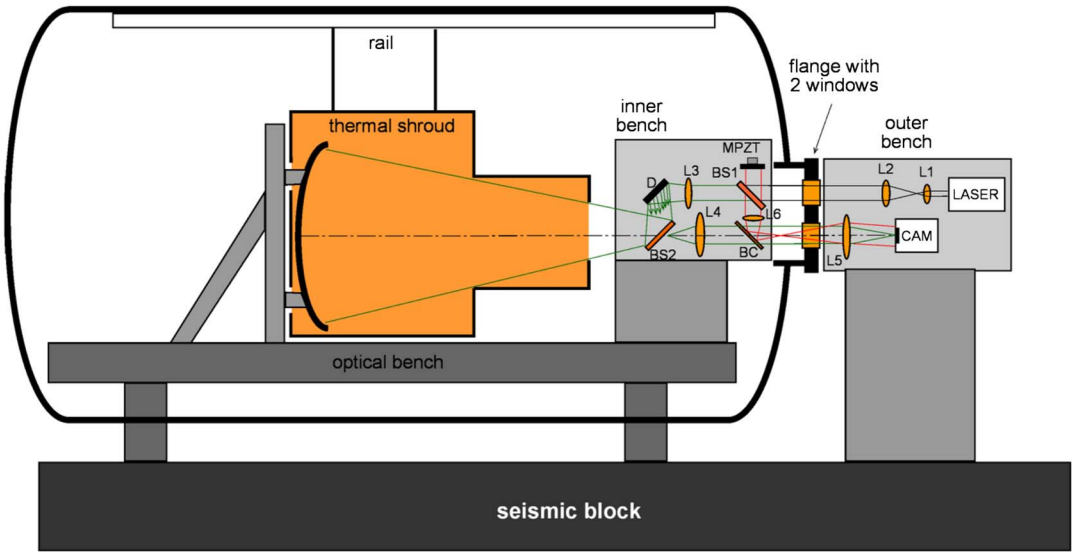

Fig. 13. (Color online) Scheme of the DH interferometer implemented in the vacuum chamber FOCAL5 of the CSL.

made use of a null lens. We compare the deformation measured with the two techniques in Fig. 15 for the same temperature range. The RMS difference is 1.6 μm, which is close to the measurement uncertainty that we found for the DH technique with diffuse illumination (Section 5).

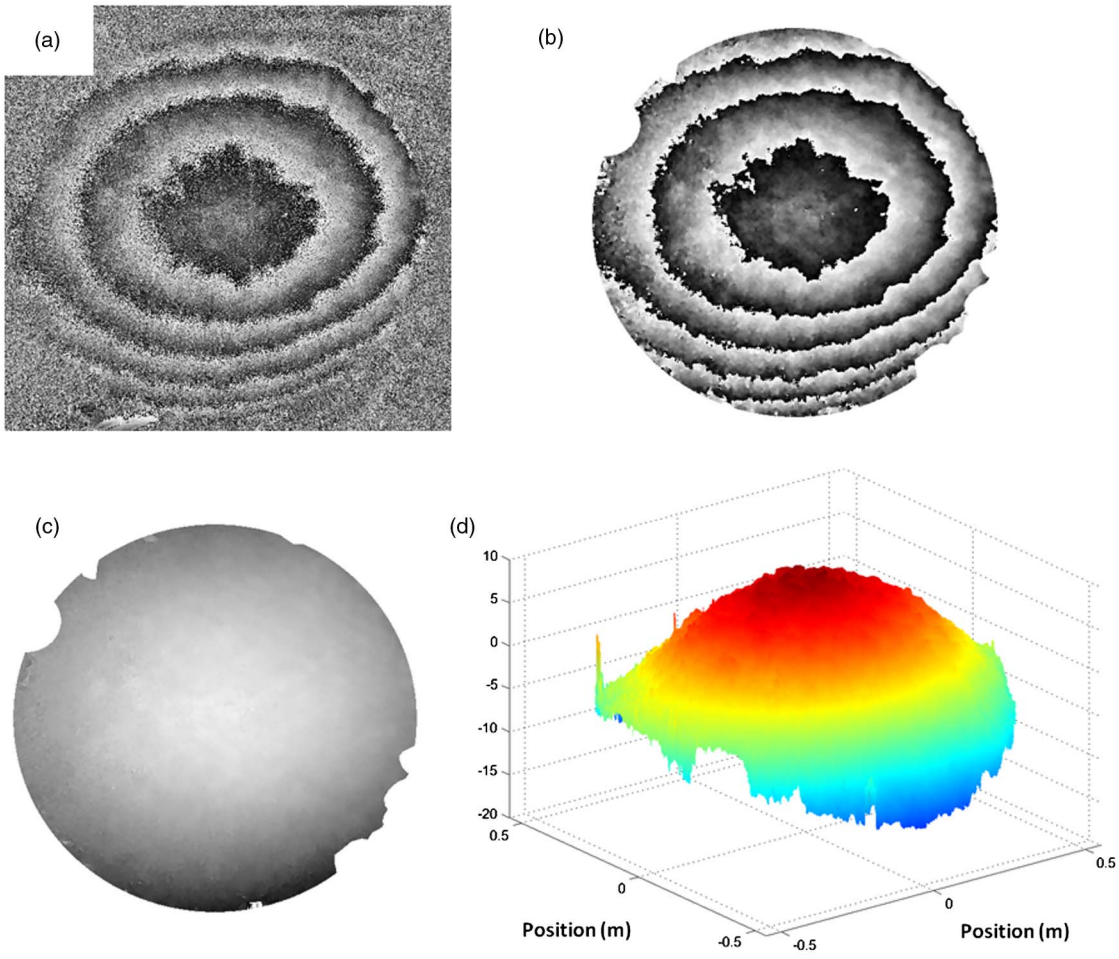

Fig. 14. (Color online) Displacement field obtained between 224 and 107.5 K. (a) Phase difference, (b) after masking and median filtering, (c) after phase unwrapping, (d) 3D plot of total displacement (Media 1 shows increasing displacement when temperature changes).

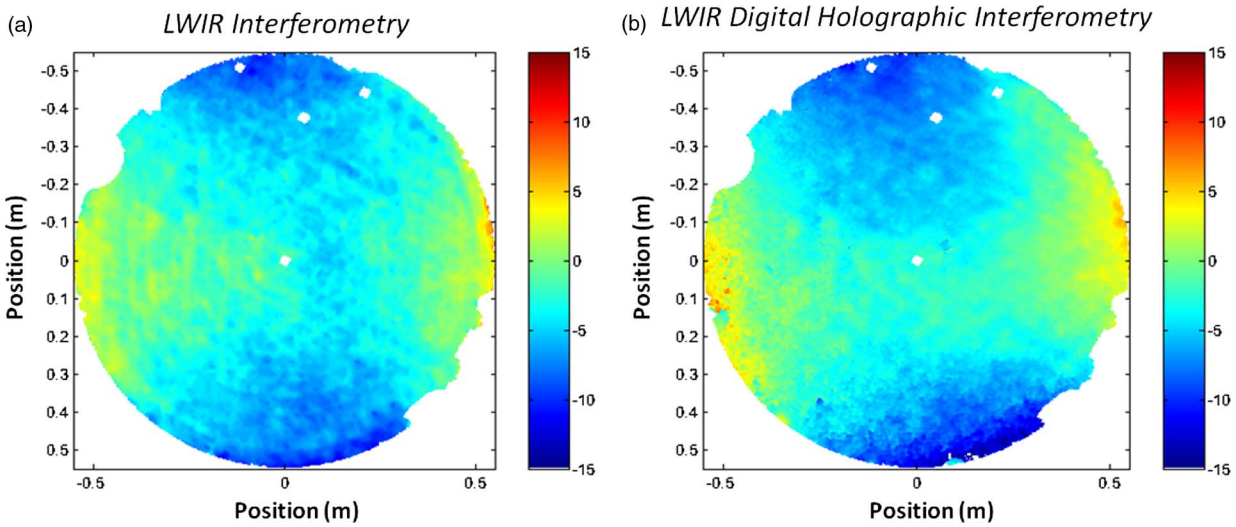

Fig. 15. (Color online) Comparison between previous results obtained (a) by LWIR interferometer with null lens and (b) DHI, both after removal of tilt and defocus showing comparable and reproducible deformations.

8. Conclusions: Future Prospects

We have presented the development of a digital holographic interferometer in the LWIR and which uses a CO_2 laser and a microbolometer array sensor. The target application is the cryogenic test of large space aspheric reflectors working in the far-infrared and submillimeter ranges.

The advantage of an LWIR digital holographic interferometer is twofold: first, it is able to measure deformations 20 times larger than similar interferometers working in the visible, and second, the stability constraint of the holographic setup is relaxed. The second advantage of LWIR DH is that is can reconstruct objects 5–10 times larger than in the visible. We have discussed some features related to the LWIR. First, an incoherent thermal background is present in the hologram, and we proposed a simple way to filter it. Second, the reflectivity appears more specular in the LWIR than in the visible. This difficulty coupled to the fact that the aspheric space reflectors are intrinsically specular led us to study the possibility of diffuse illumination. Starting from similar experiments in visible ESPI, we show that a reflective diffuse illumination can be used for illuminating specular objects that are further reconstructed numerically by DH. We first have proven this in the visible and then in the LWIR spectrum, prior to applying it to the measurement of the rotation of plane mirrors.

Then we presented in details the design of our LWIR DH interferometer, which makes use of diffuse illumination and which is used for observation of a parabolic reflector [coming from the ESA FIRST (HERSCHEL) project]. We have shown that, among the different existing DH geometries, the in-line configuration with phase shifting is the most appropriate in terms of resolution for our object. The fact that phase shifting implies a longer time of image capture is not a problem because the deformations that will be observed during cryogenic tests are much slower than the phase-shifting sequence.

After development of the DH setup and verification on the FIRST reflector in the laboratory, the whole setup and specimen was implemented in a cryogenic facility of the CSL, where vacuum-thermal cycling was operated and the deformation measured during this time. The results are found in very good agreement with similar tests performed with classical LWIR interferometry making use of null lens.

We point out here that, compared to classical null-lens interferometry, DHI allows a much simpler approach and that components of the shelf can be used. Indeed, DH can reconstruct image of object at arbitrary distances, and there is *a priori* no need of closely matching the aspheric wavefront with an expensive and dedicated optical assembly like a null lens. The diffuse illumination helps in the fact that it generates rays that can be collected easily by simple lenses and that form an object beam that can interfere with a RB in a DH setup. This simple principle opens the way for testing more complex specular reflectors, either aspheric (astigmatic or stigmatic like ellipses) or arbitrary shapes like free-form RF reflectors used for Earth telecommunications from space.

At the time of writing this paper, new experiments are ongoing for comparing the diffuse illumination with the specular case, as is discussed in Section 4. Also the case of an elliptic reflector (such as secondary reflector of the Planck telescope) will be treated as well. We also investigate the possibility of testing free-form telecommunication antenna reflectors, which is an even more challenging application.

The developments presented in this paper have been realized in the frame of the ESA General Support Technology Programme (GSTP) project, contract 22540/09/NL/SFe.

References

1. D. Malacara, ed., *Optical Shop Testing* (Wiley-VCH, 2007).
2. T. Kreis, *Handbook of Holographic Interferometry—Optical and Digital Methods* (Wiley-VCH, 2005).
3. F. Chen, G. M. Brown, and M. Song, "Overview of three-dimensional shape measurement using optical methods," Opt. Eng. **39**, 10–22 (2000).
4. M. A. Sutton, J.-J. Orteu, and H. W. Schreifer, *Image Correlation for Shape, Motion and Deformation Measurement. Basic Concepts, Theory and Applications* (Springer, 2009).
5. X. Su and Q. Zhang, "Dynamic 3-D shape measurement: a review," Opt. Lasers Eng. **48**, 191–204 (2010).
6. R. S. Pappa, J. T. Black, J. R. Blandino, T. W. Jones, P. M. Danehy, and A. A. Dorrington, "Dot-projection photogrammetry and videogrammetry of Gossamer space structures," J. Spacecr. Rockets **40**, 858–867 (2003).
7. C. S. Fraser, "Photogrammetric measurement to one part in a million," Photogramm. Eng. Remote Sens. **53**, 305–310 (1992).
8. J. A. Parian, A. Gruen, and A. Cozzani, "Monitoring of the reflectors of ESA's Planck telescope by close-range photogrammetry," J. Appl. Geodesy **1**, 137–145 (2007).
9. O. Kwon, J. C. Wyant, and C. R. Hayslett, "Rough surface interferometry at 10.6 μm," Appl. Opt. **19**, 1862–1869 (1980).
10. K. Verma and B. Han, "Far-infrared Fizeau interferometry," Appl. Opt. **40**, 4981–4987 (2001).
11. N. Ninane and A. Mazzoli, "Development of a high spatial resolution interferometer," ESA General Support Technology Programme, contract Nr 16286/02/NL/PA, Summary Rep., May 2005, available upon request to the authors.
12. http://www.esa.int/SPECIALS/Planck/index.html.
13. S. Roose, Y. Houbrechts, A. Mazzoli, N. Ninane, Y. Stockman, R. Daddato, V. Kirschner, L. Venacio, and D. de Chambure, "Cryo-optical testing of large aspheric reflectors operating in the sub mm range," Proc. SPIE **6148**, 61480F (2006).
14. N. Ninane and M. P. Georges, "Holographic interferometry using two-wavelength holography for the measurement of large deformations," Appl. Opt. **34**, 1923–1928 (1995).
15. M. P. Georges and Ph. C. Lemaire, "Real-time holographic interferometry using sillenite photorefractive crystals. Study and optimization of a transportable set-up for quantified phase measurements on large objects," Appl. Phys. B **68**, 1073–1083 (1999).
16. M. P. Georges, V. S. Scauflaire, and Ph. C. Lemaire, "Compact and portable holographic camera using photorefractive crystals. Application in various metrological problems," Appl. Phys. B **72**, 761–765 (2001).
17. C. Thizy, Y. Stockman, D. Doyle, P. Lemaire, Y. Houbrechts, M. Georges, A. Mazzoli, E. Mazy, I. Tychon, and G. Ulbrich, "Dynamic holography for the space qualification of large reflectors," Proc. SPIE **5965**, 59650W (2005).
18. C. Thizy, Y. Stockman, Ph. Lemaire, Y. Houbrechts, A. Mazzoli, M. Georges, E. Mazy, I. Tychon, D. Doyle, and G. Ulbrich, "Qualification of large reflectors in space environment with a holographic camera based on a BSO crystal," in *Photorefractive Effects, Materials, and Devices*, Vol. **99** of OSA Trends in Optics and Photonics, G. Zhang, D. Kip, D. Nolte, and J. Xu, eds. (Optical Society of America, 2005), paper 707.
19. C. Thizy, M. Georges, Ph. Lemaire, Y. Stockman, and D. Doyle, "Phase control strategies for stabilization of photorefractive holographic interferometer," Proc. SPIE **6341**, 63411O (2006).
20. J. W. Goodman and R. W. Lawrence, "Digital image formation from electronically detected holograms," Appl. Phys. Lett. **11**, 77–79 (1967).
21. U. Schnars and W. Jueptner, "Direct recording of holograms by a CCD target and numerical reconstruction," Appl. Opt. **33**, 179–181 (1994).
22. U. Schnars and W. Jueptner, "Direct phase determination in hologram interferometry with use of digitally recorded holograms," J. Opt. Soc. Am. A **11**, 2011–2015 (1994).
23. U. Schnars and W. Jueptner, *Digital Holography: Digital Hologram Recording, Reconstruction Principle, and Related Techniques* (Springer, 2005).
24. T.-C. Poon, *Digital Holography and Three-Dimensional Display* (Springer, 2006).
25. F. Dubois, N. Callens, C. Yourassowsky, M. Hoyos, P. I. Kurowski, and O. Monnom, "Digital holographic microscopy with reduced spatial coherence for three-dimensional particle flow analysis," Appl. Opt. **45**, 864–871 (2006).
26. G. Pedrini, W. Osten, and M. E. Gusev, "High-speed digital holographic interferometry for vibration measurement," Appl. Opt. **45** 3456–3462 (2006).
27. A. Faridian, D. Hopp, G. Pedrini, U. Eigenthaler, M. Hirscher, and W. Osten, "Nanoscale imaging using deep ultraviolet digital holographic microscopy," Opt. Express **18**, 14159–14164 (2010).
28. E. Allaria, S. Brugioni, S. De Nicola, P. Ferraro, S. Grilli, and R. Meucci, "Digital holography at 10.6 μm," Opt. Commun. **215**, 257–262 (2003).
29. M. S. Heimbeck, M. K. Kim, D. A. Gregory, and H. O. Everitt, "Terahertz digital holography using angular spectrum and dual wavelength reconstruction methods," Opt. Express **19**, 9192–9200 (2011).
30. R. J. Mahon, J. A. Murphy, and W. Lanigan, "Digital holography at millimetre wavelengths," Opt. Commun. **260**, 469–473 (2006).
31. J. S. Chivian, R. N. Claytor, and D. D. Eden, "Infrared holography at 10.6 μm," Appl. Phys. Lett. **15**, 123–125 (1969).
32. R. R. Roberts and T. D. Black, "Infrared holograms recorded at 10.6 μm and reconstructed at 0.6328 μm," Appl. Opt. **15**, 2018–2019 (1976).
33. W. A. Simpson and W. E. Deeds, "Real-time visual reconstruction of infrared holograms," Appl. Opt. **9**, 499–501 (1970).
34. S. Kobayashi and K. Kurihara, "Infrared holography with wax and gelatin film," Appl. Phys. Lett. **19**, 482–484 (1971).
35. G. Decker, H. Herold, and H. Röhr, "Holography and holographic interferometry with pulsed high power infrared lasers," Appl. Phys. Lett. **20**, 490–492 (1972).
36. P. R. Forman, S. Humphries, and R. W. Peterson, "Pulsed holographic interferometry at 10.6 μm," Appl. Phys. Lett. **22**, 537–539 (1973).
37. M. Rioux, M. Blanchard, M. Cormier, R. Beaulieu, and D. Bélanger, "Plastic recording media for holography at 10.6 μm," Appl. Opt. **16**, 1876–1879 (1977).
38. R. Beaulieu, R. A. Lessard, M. Cormier, M. Blanchard, and M. Rioux, "Infrared holography on commercial wax at 10.6 μm," Appl. Phys. Lett. **31**, 602–603 (1977).
39. R. Beaulieu, R. A. Lessard, M. Cormier, M. Blanchard, and M. Rioux, "Pulsed IR holography on takiwax films," Appl. Opt. **17**, 3619–3621 (1978).
40. J. Lewandowski, B. Mongeau, and M. Cormier, "Real-time interferometry using IR holography on oil films," Appl. Opt. **23**, 242–246 (1984).
41. R. Beaulieu, R. A. Lessard, and S. L. Chin, "Resist recording media for holography at 10.6 μm," Proc. SPIE **2042**, 259–263 (1994).
42. R. Beaulieu, R. A. Lessard, and S. Ling Chin, "Recording of infrared radiation (10.6 μm) in a tetrafluoroethylene copolymer of vinylidene fluoride," in *Proceedings of the International Conference on Lasers '94* (STS Press, 1994), pp. 758–762.
43. R. Beaulieu and R. A. Lessard, "Infrared holography on poly (acrylic acid) films," Proc. SPIE **4087**, 1298–1301 (2000).
44. S. Calixto, "Albumen as a relief recording media for spatial distributions of infrared radiation. fabrication of interference gratings and microlenses," Appl. Opt. **42**, 259–263 (2003).
45. O. J. Løkberg and O. Kwon, "Electronic speckle pattern interferometry using a CO_2 laser," Opt. Laser Technol. **16**, 187–192 (1984).
46. P. Picart and J. Leval, "General theoretical formulation of image formation in digital Fresnel holography," J. Opt. Soc. Am. A **25**, 1744–1761 (2008).
47. P. W. Kruse, *Uncooled Thermal Imaging. Arrays, Systems and Applications* (SPIE, 2001).
48. S. De Nicola, P. Ferraro, S. Grilli, L. Miccio, R. Meucci, P. K. Buah-Bassuah, and F. T. Arecchi, "Infrared digital reflective-holographic 3D shape measurements," Opt. Commun. **281**, 1445–1449 (2008).
49. J. L. Tissot, "IR detection with uncooled focal plane arrays. State-of-the-art and trends," Opto-Electron. Rev. **12**, 105–109 (2004).

50. N. George, K. Khare, and W. Chi, "Infrared holography using a microbolometer array," Appl. Opt. **47**, A7–A12 (2008).
51. B. Fièque, P. Robert, C. Minassian, M. Vilain, J. L. Tissot, A. Crastes, O. Legras, and J. J. Yon, "Uncooled amorphous silicon XGA IRFPA with 17 μm pixel-pitch for high end applications," Proc. SPIE **6940**, 69401X (2008).
52. J.-F. Vandenrijt and M. Georges, "Infrared electronic speckle pattern interferometry at 10 μm," Proc. SPIE **6616**, 66162Q1 (2007).
53. J.-F. Vandenrijt and M. Georges, "Electronic speckle pattern interferometry and digital holographic interferometry with microbolometer arrays at 10.6 μm," Appl. Opt. **49**, 5067–5075 (2010).
54. I. Alexeenko, J.-F. Vandenrijt, M. Georges, G. Pedrini, T. Cédric, W. Osten, and B. Vollheim, "Digital holographic interferometry by using long wave infrared radiation (CO_2 laser)," Appl. Mech. Mater. **24-25**, 147–152 (2010).
55. I. Alexeenko, J.-F. Vandenrijt, G. Pedrini, C. Thizy, B. Vollheim, W. Osten, and M. Georges, "Nondestructive testing by using long wave infrared interferometric techniques with CO_2 lasers and microbolometer arrays," Appl. Opt. **52**, A56–A67 (2013)..
56. M. Paturzo, A. Pelagotti, A. Finizio, L. Miccio, M. Locatelli, A. Geltrude, P. Poggi, R. Meucci, and P. Ferraro, "Optical reconstruction of digital holograms recorded at 10.6 μm: route for 3D imaging at long infrared wavelengths," Opt. Lett. **35**, 2112–2114 (2010).
57. A. Geltrude, M. Locatelli, P. Poggi, A. Pelagotti, M. Paturzo, P. Ferraro, and R. Meucci, "Infrared digital holography for large objects investigation," Proc. SPIE **8082**, 80820C (2011).
58. A. Pelagotti, M. Paturzo, A. Geltrude, M. Locatelli, R. Meucci, P. Poggi, and P. Ferraro, "Digital holography for 3D imaging and display in the IR range: challenges and opportunities," 3D Res. **1**, 1–10 (2010).
59. T. Kreis and W. Jüptner, "Suppression of the DC term in digital holography," Opt. Eng. **36**, 2357–2360 (1997).
60. Ø. Skotheim, "HoloVision: a software package for reconstruction and analysis of digitally sampled holograms," Proc. SPIE **4933**, 311–316 (2003).
61. I. Yamaguchi, "Fundamentals and applications of speckle," Proc. SPIE **4933**, 1–8 (2003).
62. J. C. Stover, *Optical Scattering—Measurement and Analysis* (McGraw-Hill, 1990).
63. J.-F. Vandenrijt, C. Thizy, I. Alexeenko, I. Jorge, I. López, I. Sáez de Ocáriz, G. Pedrini, W. Osten, and M. Georges, "Electronic speckle pattern interferometry at long infrared wavelengths. Scattering requirements," in *Proceedings of Fringe 2009, 6th International Workshop on Advanced Optical Metrology* (Springer, 2009), pp. 1–4.
64. R. Pawluczyk and Z. Kraska, "Diffusive illumination in holographic double-aperture interferometry," Appl. Opt. **24**, 3072–3078 (1985).
65. R. S. Hansen, "Deformation measurement of specularly reflecting objects using holographic interferometry with diffusive illumination," Opt. Lasers Eng. **28**, 259–275 (1997).
66. R. S. Hansen, "A compact ESPI system for displacement measurements of specular reflecting or optical rough surfaces," Opt. Lasers Eng. **41**, 73–80 (2004).
67. F. Dubois, L. Joannes, O. Dupont, J.-L. Dewandel, and J.-C. Legros, "An integrated optical set-up for fluid-physics experiments under microgravity conditions," Meas. Sci. Technol. **10**, 934–945 (1999).
68. http://smsc.cnes.fr/HERSCHEL/index.htm.
69. J. Mundt and T. Kreis, "Digital holographic recording and reconstruction of large objects for metrology and display," Opt. Eng. **49**, 125801 (2010).
70. T. Zhang and I. Yamaguchi, "Three-dimensional microscopy with phase-shifting digital holography," Opt. Lett. **23**, 1221–1223 (1998).
71. http://www.csl.ulg.ac.be/index.php?page=37.